



# Wireless THz link with optoelectronic transmitter and receiver

TOBIAS HARTER,<sup>1,2</sup> SANDEEP UMMETHALA,<sup>1,2</sup> MATTHIAS BLAICHER,<sup>1,2</sup> SASCHA MUEHLBRANDT,<sup>1,2</sup> STEFAN WOLF,<sup>1</sup> MARCO WEBER,<sup>1</sup> MD MOSADDEK HOSSAIN ADIB,<sup>1</sup> JUNED. N. KEMAL,<sup>1</sup> MARCO MERBOLDT,<sup>1</sup> FLORIAN BOES,<sup>3</sup> SIMON NELLEN,<sup>4</sup> AXEL TESSMANN,<sup>5</sup> MARTIN WALTHER,<sup>5</sup> BJÖRN GLOBISCH,<sup>4</sup> THOMAS ZWICK,<sup>3</sup> WOLFGANG FREUDE,<sup>1</sup> SEBASTIAN RANDEL,<sup>1</sup> AND CHRISTIAN KOOS<sup>1,2,\*</sup>

<sup>1</sup>Institute of Photonics and Quantum Electronics (IPQ), Karlsruhe Institute of Technology (KIT), 76131 Karlsruhe, Germany

<sup>2</sup>Institute of Microstructure Technology (IMT), Karlsruhe Institute of Technology (KIT), 76344 Eggenstein-Leopoldshafen, Germany

<sup>3</sup>Institute of Radio Frequency Engineering and Electronics (IHE), Karlsruhe Institute of Technology (KIT), 76131 Karlsruhe, Germany

<sup>4</sup>Fraunhofer Institute for Telecommunications, Heinrich Hertz Institute (HHI), 10587 Berlin, Germany

<sup>5</sup>Fraunhofer Institute for Applied Solid State Physics (IAF), 79108 Freiburg, Germany

\*Corresponding author: christian.koos@kit.edu

Received 5 December 2018; revised 21 May 2019; accepted 2 July 2019 (Doc. ID 353246); published 13 August 2019

Photonics might play a key role in future wireless communication systems that operate at terahertz (THz) carrier frequencies. A prime example is the generation of THz data streams by mixing optical signals in high-speed photo-detectors. Over previous years, this concept has enabled a series of wireless transmission experiments at record-high data rates. Reception of THz signals in these experiments, however, still relied on electronic circuits. In this paper, we show that wireless THz receivers can also greatly benefit from optoelectronic signal processing techniques, in particular when carrier frequencies beyond 0.1 THz and wideband tunability over more than an octave is required. Our approach relies on a high-speed photoconductor and a photonic local oscillator for optoelectronic downconversion of THz data signals to an intermediate frequency band that is easily accessible by conventional microelectronics. By tuning the frequency of the photonic local oscillator, we can cover a wide range of carrier frequencies between 0.03 and 0.34 THz. We demonstrate line rates of up to 10 Gbit/s on a single channel and up to 30 Gbit/s on multiple channels transmitted over a distance of 58 m. To the best of our knowledge, our experiments represent the first demonstration of a THz communication link that exploits optoelectronic signal processing techniques both at the transmitter and the receiver. © 2019 Optical Society of America under the terms of the OSA Open Access Publishing Agreement

<https://doi.org/10.1364/OPTICA.6.001063>

## 1. INTRODUCTION AND BACKGROUND

Data traffic in wireless communication networks is currently doubling every 22 months [1] and will account for more than 70% of the overall internet traffic by 2022. Sustaining this growth requires advanced network architectures that combine massive deployment of small radio cells [2–4] with powerful backhaul infrastructures that exploit high-capacity wireless point-to-point links. Such links may be efficiently realized by exploiting THz carriers in low-loss atmospheric transmission windows [5], thereby offering data rates of tens or even hundreds of Gbit/s. To generate the underlying communication signals at the THz transmitter (Tx), optoelectronic signal processing [6–11] has emerged as a particularly promising approach, leading to demonstrations of wireless transmission at line rates of 100 Gbit/s and beyond [12–18]. At the THz receiver (Rx), however, the advantages of optoelectronic signal processing have not yet been exploited.

In this paper, we show that wireless THz Rx can benefit from optoelectronic signal processing techniques as well, in particular when carrier frequencies beyond 0.1 THz and wideband tunability are required [19,20]. We exploit a high-speed photoconductor and a photonic local oscillator (LO) for terahertz-to-electrical downconversion over a broad range of frequencies between 0.03 and 0.34 THz. In our experiments, we demonstrate a coherent wireless link that operates at a carrier frequency of 0.31 THz and allows line rates of up to 10 Gbit/s on a single channel and up to 30 Gbit/s on multiple channels, transmitted over a distance of 58 m. To the best of our knowledge, this represents the first demonstration of a THz communication link that complements optoelectronic signal generation at the Tx by optoelectronic downconversion at the Rx.

The vision of a future wireless network architecture is shown in Fig. 1(a). The increasing number of terminal devices and the advent of new data-hungry applications require a dense mesh of

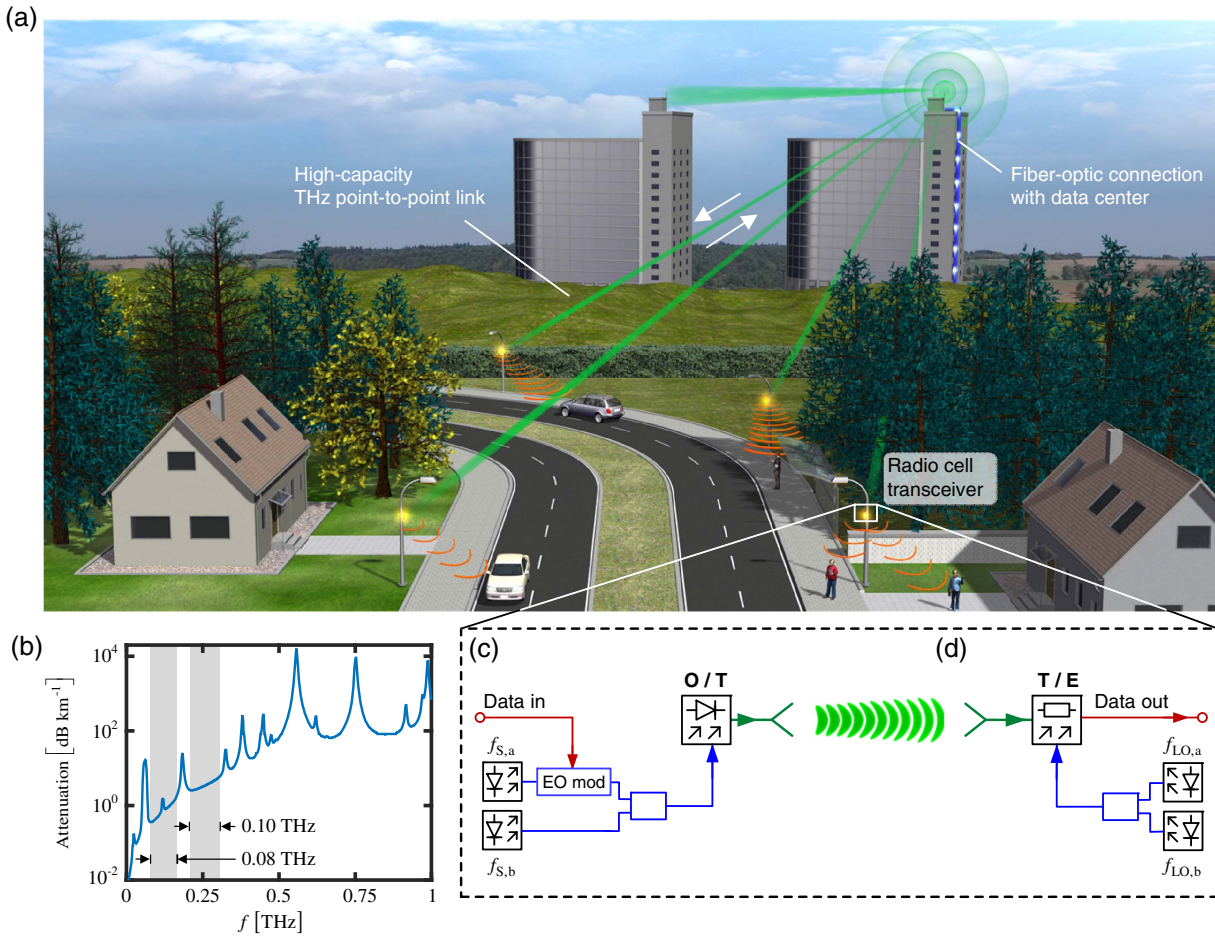


**Fig. 1.** T-wave wireless infrastructure using optoelectronic signal processing techniques. (a) Vision of a future wireless network architecture. A dense mesh of small radio cells provides broadband wireless access to a vast number of users and devices. The high data rates required for the underlying wireless backhauling infrastructures are provided by high-speed wireless point-to-point links that are operated at THz frequencies and that can be efficiently interfaced with fiber-optic networks. (b) T-wave atmospheric attenuation [23] for standard conditions (temperature of 15°C, water vapor content of 7.5 g/m<sup>3</sup>). Various windows with low attenuation can be used for T-wave communications. Our Rx allows operation over a wide range of frequencies between 0.03 and 0.34 THz, in which the atmospheric attenuation is small enough to permit transmission over technically relevant distances. (c) Optoelectronic T-wave signal generation. The data signal is modulated on an optical c.w. tone with frequency  $f_{S,a}$  by an electro-optic modulator (EO mod). The modulated signal is superimposed with an unmodulated c.w. tone  $f_{S,b}$ , and the optical signal is converted to a T-wave signal in a high-speed photodiode (O/T), where the carrier frequency of the T-wave is given by the frequency difference  $f_S = |f_{S,a} - f_{S,b}|$ . The T-wave is radiated into free space by an antenna. (d) Optoelectronic coherent T-wave reception. The T-wave data signal is downconverted in a photoconductor where the optical power beat  $f_{LO} = |f_{LO,a} - f_{LO,b}|$  of two unmodulated c.w. tones acts as photonic local oscillator (T/E).

small radio cells to provide ubiquitous broadband wireless access [2–4]. Backhauling of these cells relies on high-speed wireless point-to-point links, which are seamlessly integrated into fiber-optic networks [21,22]. The high data rates required for wireless backhauling infrastructures are achieved by using carrier frequencies in the range of 0.1–1 THz (T-waves). Figure 1(b) shows the atmospheric T-wave attenuation as a function of frequency [23], revealing several transmission windows with low loss that can be used for wireless communications. For highest flexibility and performance, T-wave Tx and Rx should be able to switch between various windows depending on channel occupancy and weather conditions. At the Tx, this can be achieved by optoelectronic T-wave signal generation [Fig. 1(c)], which relies on mixing of an optical data signal at a carrier frequency  $f_{S,a}$  with a continuous-wave (c.w.) tone at a frequency  $f_{S,b}$  in a high-speed photodiode (optical-to-T-wave, O/T conversion). This leads to a T-wave data signal centered at the carrier frequency  $f_S = |f_{S,a} - f_{S,b}|$ , which can

be widely tuned by changing the frequency  $f_{S,b}$  of the unmodulated optical tone. Note that similar optoelectronic Tx concepts have been used in earlier demonstrations [12–17], but were complemented by an electronic Rx that cannot match the wideband tunability of the Tx. To overcome this limitation, we have implemented an optoelectronic Rx that requires neither an electronically generated local oscillator nor an electronic mixer for coherent reception, but relies on a photoconductor that is driven by a photonic LO instead [Fig. 1(d)]. The photonic LO is generated by superimposing two optical c.w. tones with frequencies  $f_{LO,a}$  and  $f_{LO,b}$  and coupling them to the photoconductor [24–26] for downconversion of the T-wave data signal to an intermediate frequency band that is easily accessible by conventional microelectronics (T-wave-to-electric, T/E conversion). Note that optically driven photoconductors have previously been used for downconversion of T-waves in spectroscopy systems [24–28]. These demonstrations, however, are usually based on T-wave Tx and Rx that

are driven by a common pair of lasers ( $f_{S,a} = f_{LO,a}$ ,  $f_{S,b} = f_{LO,b}$ ) for homodyne reception, and they rely on narrowband detection schemes with typical averaging times of the order of 1 ms. This corresponds to bandwidths of a few kilohertz and allows for highly sensitive reception of small T-wave power levels. In our work, we advance these concepts to enable wireless data transmission at gigahertz bandwidth over technically relevant distances, using amplitude and phase-modulated T-wave carriers for transmitting information. To this end, we make use of advanced photoconductors with engineered carrier lifetime [22], and we mount them together with high-speed transimpedance amplifiers (TIAs) [29] in a metal housing. We exploit heterodyne detection in combination with advanced digital signal processing to overcome phase noise and frequency drift associated with the free-running photonic LO at the Rx. In the following, we discuss the details of the optoelectronic Rx module, and we demonstrate a T-wave communication system.

## 2. IMPLEMENTATION OF OPTOELECTRONIC RX

The concept and the implementation of the optoelectronic Rx is illustrated in Fig. 2(a). The T-wave data signal, oscillating at an angular carrier frequency  $\omega_S = 2\pi f_S$ , is received by a bow-tie antenna, resulting in a T-wave voltage  $U(t)$  across the antenna feed points:

$$U(t) = \hat{U}_S(t) \cos(\omega_S t + \varphi_S(t)). \quad (1)$$

In this relation,  $\hat{U}_S(t)$  is the modulated T-wave voltage amplitude, and  $\varphi_S(t)$  is the associated modulated phase. The antenna feed points are connected to the photoconductor  $G$ , which is illuminated by the photonic LO that provides a time-dependent optical power. The optical power oscillates at a frequency  $\omega_{LO} = 2\pi|f_{LO,a} - f_{LO,b}|$  with amplitude  $\hat{P}_{LO,1}$  and phase  $\varphi_{P,LO}$ :

$$P_{LO}(t) = P_{LO,0} + \hat{P}_{LO,1} \cos(\omega_{LO} t + \varphi_{P,LO}). \quad (2)$$

The free carriers generated by the absorbed optical power change the photoconductance according to

$$G(t) = \mathcal{G}P_{LO}(t) = G_0 + \hat{G}_{LO} \cos(\omega_{LO} t + \varphi_{LO}), \quad (3)$$

where  $\mathcal{G}$  denotes a proportionality constant that describes the sensitivity of the photoconductor. Note that the phase  $\varphi_{LO}$  of the conductance oscillation might differ from the phase of the optical power oscillation  $\varphi_{P,LO}$  if the period of the LO power oscillation is of the same order of magnitude as the lifetime of the free carriers of the photoconductor. The resulting current  $I(t)$  through the photoconductor is given by the product of the time-varying conductance  $G(t)$  and the T-wave voltage  $U(t)$ , leading to mixing of the T-wave signal centered around  $\omega_S$  and the optical LO power oscillating at  $\omega_{LO}$ . After processing of the current by subsequent electronics, such as a TIA, only the low-frequency components of the mixing product remain, leading to a downconverted current at an intermediate frequency  $\omega_{IF} = |\omega_S - \omega_{LO}|$ :

$$I_{IF}(t) = \frac{1}{2} \hat{G}_{LO} \hat{U}_S(t) \cos(\omega_{IF} t + \varphi_S(t) - \varphi_{LO}). \quad (4)$$

This intermediate signal contains the amplitude and phase information of the T-wave data signal. A more detailed derivation of Eqs. (1)–(4) can be found in Supplement 1, Section 1.

Figure 2(b) illustrates the technical implementation of the Rx module used for our experiments. The photoconductor [24] is connected to a bow-tie antenna, which is electrically coupled to a TIA by a metal wire bond. The photoconductor is operated without any additional DC bias, and a decoupling capacitor  $C = 1$  nF is used to isolate the device from the bias that is effective at the input of the TIA; see Supplement 1, Section 2. The output of the TIA is electrically connected to a printed circuit board (PCB). The photoconductor is illuminated from the top with the optical power  $P_{LO}(t)$ , which is coupled to the device from the horizontally positioned fiber by a photonic wire bond [30]. The entire assembly is glued onto a silicon lens that captures the T-wave signal incoming from the bottom and focuses it to the antenna on the chip surface; see Fig. 2(c). The assembly is placed in a metal housing for effective electromagnetic shielding. A microscope image of the fabricated device and a more detailed description of the Rx module in terms of conversion efficiency, bandwidth, and noise can be found in Supplement 1, Section 2.

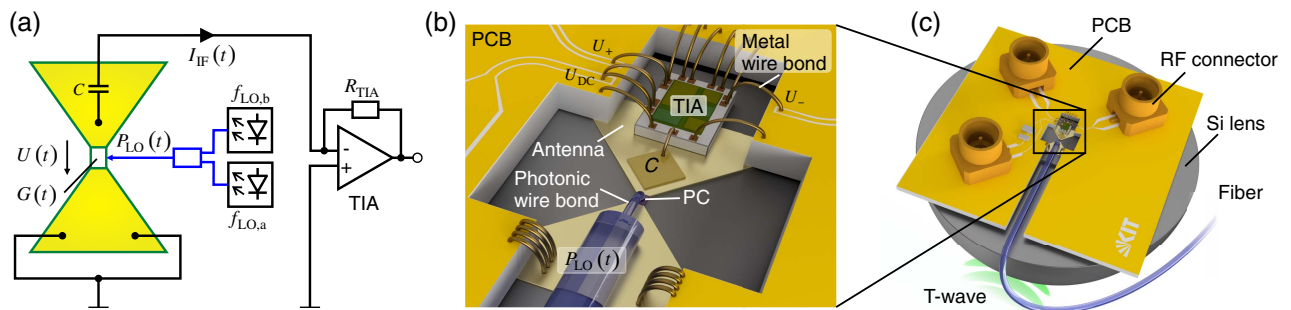


**Fig. 2.** Concept and implementation of the optoelectronic coherent T-wave Rx. (a) Schematic of the Rx. The T-wave signal centered around a carrier frequency  $f_S$  is received by a bow-tie antenna with a photoconductor between the antenna feed points. This leads to a T-wave voltage signal  $U(t)$  applied to the photoconductor. At the same time, the photoconductance  $G(t)$  is modulated at a frequency  $f_{LO}$  by the power beat of two unmodulated laser tones,  $f_{LO} = |f_{LO,a} - f_{LO,b}|$ . The two effects combined lead to a downconverted current  $I_{IF}(t)$  oscillating at the difference frequency  $|f_S - f_{LO}|$ . The current is amplified by a TIA having a transimpedance  $R_{TIA}$ . The capacitor  $C = 1$  nF blocks direct currents at the input circuit of the TIA. (b) Schematic of Rx module. The photoconductor (PC) and the antenna are electrically connected to the input of the TIA by metal wire bonds. The differential outputs of the TIA ( $U_+$  and  $U_-$ ) are connected to a PCB, realized as a gold-plated alumina ceramic substrate that includes RF connectors to feed the signals to a high-speed oscilloscope for further analysis. The photoconductor is illuminated with the optical power  $P_{LO}(t)$  by a fiber and a 3D-printed photonic wire bond. (c) The Rx assembly of photoconductor, antenna, TIA, and PCB is glued onto a silicon lens. This lens captures the T-wave signal incoming from the bottom and focuses it to the antenna on the surface of the photoconductor chip.

### 3. DEMONSTRATION OF WIRELESS THZ LINKS

In the following we demonstrate the viability of our Rx concept in a series of experiments, covering both single-channel and multi-channel transmission of THz data signals. For the single-channel experiments, our focus was on demonstrating the wideband tunability of the carrier frequency. The multi-channel experiment shows the scalability of the approach toward high-throughput parallel transmission.

#### A. Single-Channel Transmission and Wideband Tunability

The wireless transmission system for single-channel transmission is illustrated in Fig. 3(a). As a data source we use an arbitrary-waveform generator (AWG), which provides a quadrature phase-shift-keying (QPSK) signal to an optical in-phase/quadrature phase (I/Q) modulator. The modulator is fed with an optical carrier at frequency  $f_{S,a}$  generated by a tunable laser. The modulated data signal is superimposed with an unmodulated optical carrier at frequency  $f_{S,b}$ . The optical power spectrum of the data signal and the unmodulated laser tone for a 3 Gbd QPSK signal and a frequency spacing of  $f_S = |f_{S,a} - f_{S,b}| = 0.310$  THz is shown in Inset 1 of Fig. 3(a). For O/T conversion, the superimposed optical signals are fed to a commercially available uni-traveling-carrier photodiode [31] (UTC-PD). The T-wave signal is then radiated into free space by a horn antenna, and a subsequent THz lens made from polytetrafluoroethylene (PTFE) collimates the radiation. The transmission distance amounts to 58 m and is limited only by the size of our building. At the Rx, we use another lens and a horn antenna to couple the T-wave signal into a WR 3.4 hollow waveguide that is connected to a two-stage

T-wave amplifier [32]. At the output of the amplifier, another horn antenna is used to feed the signal to the photoconductor via a silicon lens and a bow-tie antenna that is co-integrated with the device. For T/E conversion, the photoconductor is illuminated by a photonic LO; see the power spectrum in Inset 2 of Fig. 3(a). A comprehensive description of the transmission setup is given in Supplement 1, Section 3, and a discussion of the link budget as well as of the noise contributions of T-wave amplifiers and the baseband circuits can be found in Supplement 1, Section 5. The total gain of the two-stage T-wave amplifier ranges from 42 to 49 dB in a frequency range from 0.260 to 0.335 THz, thereby overcompensating the loss of the 58-m-long free-space link. The noise figure of the amplifier cascade amounts to approximately 10 dB; see Supplement 1, Section 4 for details.

The output signal of the photoconductor is fed to a TIA [see Fig. 2(b)], and the amplified signals are then recorded by a real-time oscilloscope (Osc.) and stored for offline digital signal processing (DSP). The T-wave Rx relies on a heterodyne detection scheme ( $f_S \neq f_{LO}$ ), where the photonic LO is placed at the edge of the T-wave data spectrum, which leads to electrical signals centered around the intermediate frequency  $f_{IF} = |f_S - f_{LO}|$ . The in-phase and quadrature components of the QPSK baseband signals are then extracted from the intermediate signals by DSP, comprising standard procedures such as digital frequency down-conversion, timing recovery, constant-modulus equalization, frequency offset compensation, and carrier phase estimation.

Figure 3(b) shows the bit error ratio (BER) measured for various line rates  $R_b$  at a carrier frequency of 0.31 THz. For line rates below 3 Gbit/s, no errors are measured in our recording length of  $10^5$  symbols, demonstrating the excellent performance of the

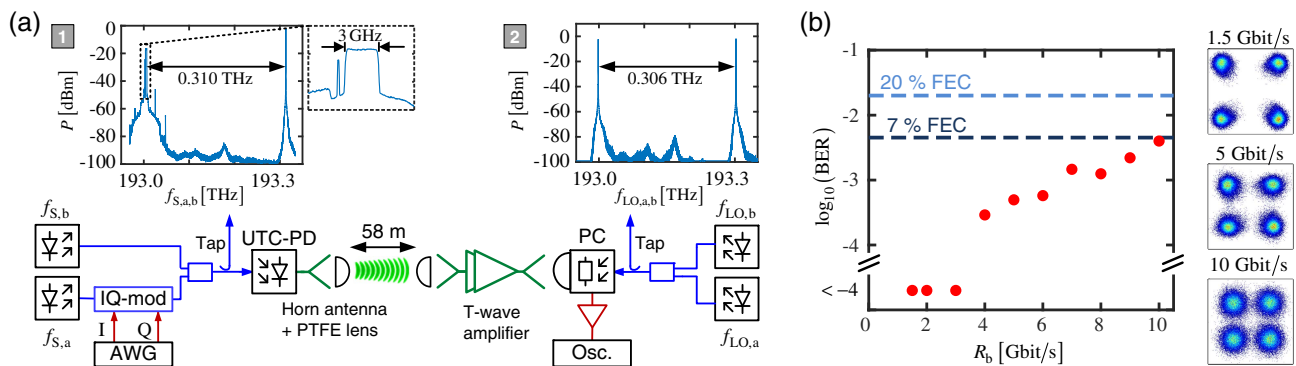


**Fig. 3.** Experimental demonstration of T-wave wireless transmission. (a) Experimental setup. At the Tx, an optical QPSK signal at a carrier frequency  $f_{S,a}$  is generated by an I/Q modulator driven by an AWG. The optical signal is then superimposed with an unmodulated optical c.w. tone at frequency  $f_{S,b}$  and converted to a T-wave data signal by a high-speed UTC-PD. The T-wave is radiated into free space by a horn antenna and a subsequent PTFE lens. The frequency of the T-wave carrier depends on the frequency difference of the lasers  $f_S = |f_{S,a} - f_{S,b}| = 0.310$  THz. At the Rx, two c.w. laser tones with frequencies  $f_{LO,a}$  and  $f_{LO,b}$  are superimposed to generate an optical power beat, which acts as a LO (photonic LO) for coherent downconversion of the T-wave by an antenna-coupled photoconductor. The wireless transmission link spans a distance of 58 m. To compensate for the transmission loss, we use a two-stage T-wave amplifier in front of the Rx. The received data signal is recorded by a real-time oscilloscope (Osc.) and offline digital signal processing is used to analyze the data. Inset 1: Optical spectrum (180 MHz resolution bandwidth, RBW) at the Tx for a 3 Gbd QPSK data stream and a T-wave carrier frequency of  $f_S = 0.310$  THz. The spectrum was recorded after a monitoring tap (Tap) introduces an attenuation of 12 dB. The overall optical power entering the UTC-PD amounts to 12.8 dBm (19 mW). Inset 2: Optical spectrum (180 MHz RBW) of the photonic LO at the Rx for  $f_{LO} = 0.306$  THz. The spectrum was recorded after an optical tap introduces an attenuation of 18 dB. The overall optical power coupled to the photoconductor amounts to 19 dBm (80 mW). (b) Measured BER for QPSK data streams with various line rates  $R_b$  transmitted at a T-wave carrier frequency of around 0.310 THz. For line rates up to 10 Gbit/s, a BER below the threshold for FEC with 7% overhead is achieved. For the data points shown at the bottom ( $\log_{10}(\text{BER}) < -4$ ), no errors were measured in our recording length of  $10^5$  symbols. Constellation diagrams for selected data rates of 1.5, 5, and 10 Gbit/s are shown on the right. Note that for an optical input power of 19 mW into the UTC-PD at the Tx, the T-wave power received by the Rx horn antenna after the free-space link was already sufficient to partially saturate the T-wave amplifier cascade. This leads to an asymmetric distribution of the noise around the various constellation points at 1.5 Gbit/s, where the limited TIA bandwidth does not play a role.

optoelectronic Rx. The constellation diagrams for line rates of 1.5, 5, and 10 Gbit/s are shown in the insets. For larger line rates, the received signal quality decreases mainly due to limitations of the TIA in the intermediate-frequency circuit. The TIA has a specified bandwidth of only 1.4 GHz, and larger line rates would require a more broadband device. With the current TIA, we could transmit 10 Gbit/s with a BER below the threshold of forward-error correction (FEC) with 7% overhead. Note that in these experiments, the T-wave power received by the horn antenna after the free-space link was already sufficient to partially saturate the T-wave amplifier cascade. This leads to an asymmetric distribution of the noise around the various constellation points at low data rates, where the limited TIA bandwidth does not play a role [see Fig. 3(b)]. A more detailed discussion of T-wave amplifier saturation can be found in Supplement 1, Section 3. Note also that the transmission distance of 58 m was dictated by space limitations. With the current components, it would be possible to bridge at least twice the distance by increasing the optical power at the Tx and by using slightly lower input power levels at the Rx to avoid saturation of the T-wave amplifier cascade.

To the best of our knowledge, our experiments represent the first demonstration of a THz transmission link that complements optoelectronic generation of T-wave signals at the Tx by optoelectronic downconversion at the Rx. Similar schemes have also been demonstrated [33,34] at lower carrier frequencies, relying on a UTC-PD for optoelectronic T/E conversion. Using this Rx, a line rate of 5 Gbit/s at a carrier frequency of 35.1 GHz and a line rate of 1 Gbit/s at a carrier frequency of 60 GHz have been demonstrated with transmission distances of 1.3 and 0.55 m, respectively. Our work relies on photoconductors with excellent linearity both with respect to the voltage and the applied optical power [19,20] and clearly demonstrates the vast potential of optoelectronic downconversion for T-wave communications at tens of Gbit/s over extended distances. To further demonstrate the flexibility of the optoelectronic Rx, we transmit 2 Gbit/s data streams at various carrier frequencies covering the entire range between 0.03 and 0.34 THz. Note that the setup shown in Fig. 3(a) allows us to address only the frequency range between 0.24 and 0.34 THz due to bandwidth limitations of both the UTC-PD and the T-wave amplifiers. For transmission at frequencies between 0.03 and 0.18 THz, we therefore omitted the amplifiers and replaced the UTC-PD by a pin photodiode (pin-PD). The measured BER and some exemplary constellation diagrams of the transmission experiments are shown in Fig. 4. For carrier frequencies between 0.24 and 0.34 THz, no errors were measured in our recordings, such that we can only specify an upper limit of  $10^{-4}$  for the BER. For carrier frequencies between 0.03 and 0.18 THz, comparable performance was obtained. For simplicity, the transmission experiments in the lower frequency range were performed over a transmission distance of 7 cm only, which could be bridged without any amplifiers. The range could be easily extended to tens or hundreds of meters by using Rx antennas that are optimized for lower frequencies in combination with amplifiers. Note also that the data points between 0.03 and 0.18 THz were taken on a slightly irregular frequency grid, thereby avoiding some carrier frequencies for which the free-space link of our setup features low transmission. This does not represent a fundamental problem and was caused by fading due to uncontrolled reflections in the beam path. The associated power variations could be overcome by using amplifiers with adaptive gain or by optimizing

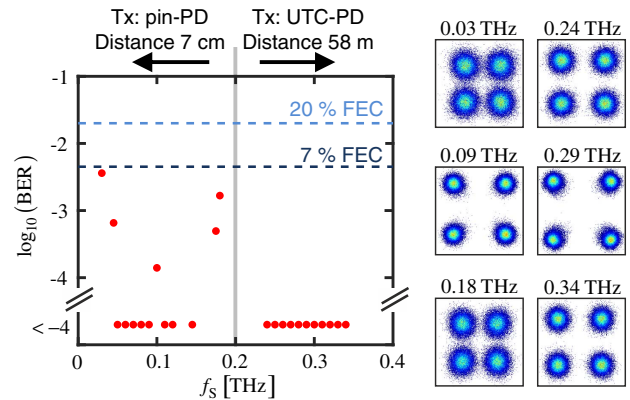


**Fig. 4.** BER and constellation diagrams for various carrier frequencies at a line rate of  $R_b = 2$  Gbit/s. For the Tx we used two different types of photodiodes depending on the T-wave frequency. For T-wave frequencies  $0.03 \text{ THz} \leq f_s \leq 0.18 \text{ THz}$  we use a lens-coupled pin-PD. For simplicity, the transmission experiments in this frequency range were performed over a reduced transmission distance of only 7 cm, which could be bridged without any amplifiers. For T-wave frequencies  $0.24 \text{ THz} \leq f_s \leq 0.34 \text{ THz}$ , a waveguide-coupled UTC-PD is used in combination with a cascade of two T-wave amplifiers, as described in Fig. 3. In both cases, the same Rx module as in Fig. 2 was used, demonstrating its exceptional wideband tunability.

the beam path for each Tx frequency point individually. This fading in combination with frequency-dependent Tx power and a decreasing gain of the on-chip bow-tie antenna for low frequencies is also the reason for the degraded performance of the transmission experiments at carrier frequencies of 0.03, 0.04, 0.10, and 0.18 THz. Still, these experiments demonstrate that the same Rx concept as in Fig. 2 can be used for carrier frequencies in a range of  $0.03 \text{ THz} \leq f_s \leq 0.340 \text{ THz}$ , i.e., over more than a decade.

## B. Multi-Channel Transmission

We also investigate the Rx in a multicarrier transmission experiment at carrier frequencies between 0.287 and 0.325 THz. We simultaneously transmit up to 20 T-wave channels (Ch 1 ... 20) spaced by 2 GHz, where each channel is operated with independent QPSK signals at a symbol rate (line rate) of 0.75 GBD (1.5 Gbit/s). To keep the experimental setup simple, we use a single broadband AWG and a single I/Q modulator to generate an optical signal that simultaneously contains all channels, which is then converted to the THz range by a UTC-PD. This approach allows us to re-use the experimental setup shown on Fig. 3(a). Alternatively, multiple optical carriers and less broadband devices in combination with optical multiplexing could have been used to generate the optical channels [14]. Figure 5(a) shows the optical spectrum containing all 20 channels, measured at the monitoring tap before the UTC-PD. To compensate for the spectral roll-off of the UTC-PD and the T-wave amplifiers, the channels at the edges of the T-wave transmission band are pre-emphasized [see inset of Fig. 5(a)]. Figure 5(b) shows the spectrum of the two optical lines, which are used as photonic LO for reception of Ch 20, which features the highest THz carrier frequency of  $f_s = 0.325 \text{ THz}$ . Note that we again used heterodyne detection at the Rx and hence chose a T-wave LO frequency  $f_{LO} = 0.326 \text{ THz}$  close to the spectral edge of Ch 20. It is also worth mentioning that the 0.75 GBD T-wave channels were transmitted

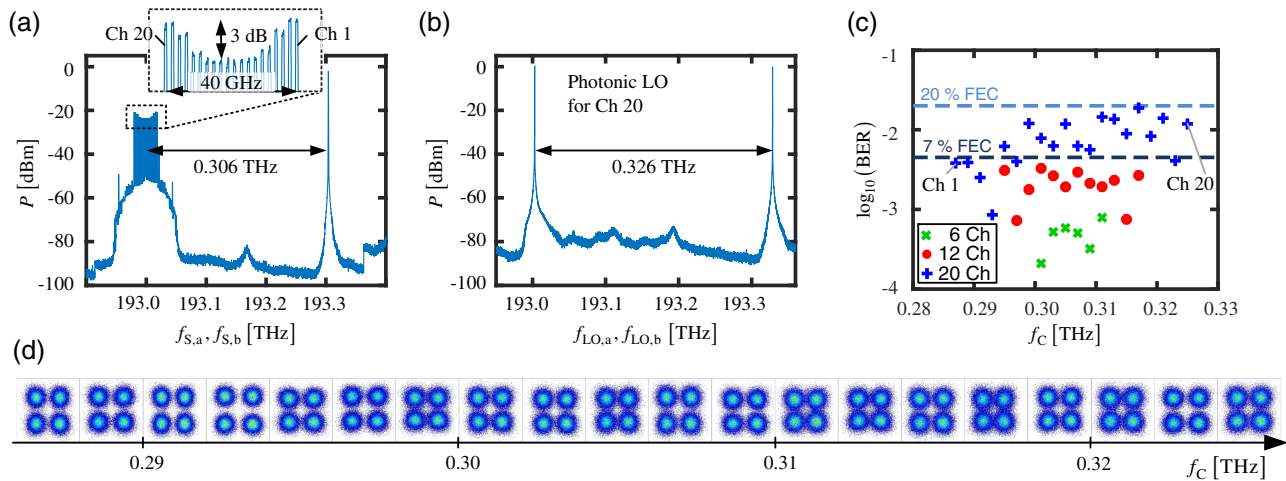


**Fig. 5.** Multi-channel T-wave transmission. (a) Optical spectrum (180 MHz RBW) at the Tx for a signal containing 20 channels. Each channel is modulated with pulses having a raised-cosine spectrum with a roll-off factor of 0.1 and carries a 0.75 Gbd QPSK signal. The channels are spaced by 2 GHz. In the UTC-PD, the channels are simultaneously downconverted to a T-wave frequency band centered at 0.306 THz. The spectrum was recorded at the optical monitoring tap after the power combiner at the Tx [Fig. 3(a)], introducing an attenuation of 12 dB. The overall optical power contained in the spectrum amounts to 12.7 dBm (18.5 mW). (b) Optical LO spectra (180 MHz RBW) at the Rx for detection of Ch 20. For heterodyne detection, the T-wave LO frequency  $f_{LO} = 0.326$  THz is chosen close to the spectral edge of the channel. The spectrum was recorded at the optical monitoring tap after the power combiner at the Rx, which introduces an attenuation of 16 dB. The overall optical power contained in the spectrum amounts to 19 dBm (80 mW). (c) Measured BER for various numbers of channels. For 12 (20) channels, the BER is below the 7% (20%) threshold for FEC. This corresponds to an aggregate line rate of 18 Gbit/s (30 Gbit/s). (d) Constellation diagrams for all 20 channels leading to an aggregate line rate of 30 Gbit/s.

on a 2 GHz grid to avoid interference of data signals from neighboring channels after downconversion to the intermediate frequency band. This leads to unused spectral regions of approximately 1.2 GHz between the T-wave channels, which could be avoided by optoelectronic downconversion schemes that allow simultaneous extraction of the in-phase and quadrature components of the T-wave signal. Figure 5(c) shows the BER for transmission experiments with six, 12, and 20 channels. For transmission of 12 channels (aggregate line rate 18 Gbit/s), the BER stays below the 7% FEC limit, whereas for 20 channels (30 Gbit/s), 20% FEC overhead is required. Figure 5(d) shows the constellation diagrams of the 20-channel experiment. The BER degradation with increasing channel count is caused mainly by the fact that the overall power available at the output of the Rx T-wave amplifier cascade is limited. A higher number of channels thus leads to a reduced power per channel and, hence, to a reduced signal-to-noise power ratio (SNR). Compared to the single-channel transmission experiment, we expect an SNR reduction of 7.8, 10.8, and 13 dB, respectively, through the splitting of the power among six, 12, and 20 channels. This is in good agreement with our measurement, where we find SNR reductions of approximately 6.5, 9.8, and 12.3 dB, respectively; see Supplement 1, Section 3 for details. Note that the different channels in our multi-channel experiments were measured sequentially. While this is a usual approach in multi-channel THz transmission experiments [13,14,18], parallel reception of the entire data stream would be desirable. In this context, T-wave demultiplexers might become highly relevant in the future [35,36].

**C. Potential for Further Improvements**

While optoelectronic signal processing features a series of conceptual advantages, such as wideband tunability of the carrier frequency and the ability to address high carrier frequencies at

hundreds of GHz, the data rates demonstrated in our proof-of-concept experiments are still smaller than those achieved with best-in-class all-electronic devices. Competing all-electronic approaches may, e.g., rely on advanced millimeter-wave integrated circuits (MMIC) operating in the V-band (57 ... 66 GHz) or the E-bands (71 ... 76 GHz and 81 ... 86 GHz) [37]. For single-input–single-output (SISO) transmission in this frequency range, impressive data rates of up to 80 Gbit/s were demonstrated [38] using a transmission bandwidth of approximately 20 GHz centered at a carrier frequency of 77 GHz. In this context, it is important to note that the data rate of 30 Gbit/s achieved by our proof-of-concept experiment is a first step but represents by no means the highest achievable performance and leaves substantial room for further improvements both on a device and a system level.

The main limitation of the current implementation is the small conversion efficiency of the photoconductor, ranging between -51 and -64 dB, depending on the carrier frequency and power of the photonic LO; see Supplement 1, Section 2. Improving the conversion efficiency is subject to current research [24,39] and might drastically enhance the performance of the optoelectronic Rx. In this context, plasmonic photoreceivers with strongly bias-dependent responsivity [9,40] might be a particularly compact alternatives to conventional photoconductors. Note that the conversion efficiency specified for our current experiment also includes the coupling losses introduced by the free-space section between the output of the T-wave amplifier cascade and the photoconductor; see Supplement 1, Section 5 for details. Co-integrating or co-packaging of the T-wave amplifiers and the subsequent photoconductor using, e.g., hollow waveguides in metallic split-block assemblies [41] could not only avoid these losses, but also improve the spectral uniformity of the Rx characteristics. Further improvements are expected from

constantly improving T-wave amplifiers and TIA. Specifically, the per-channel symbol rate in our current experiments was limited only by the bandwidth of the TIA. Using more broadband devices [42], symbol rates of more than 25 Gbd may be achieved in the future. Photoconductors with increased conversion efficiency, improved T-wave amplifiers with higher saturation output power, and faster TIA with optimized baseband circuitry could allow more broadband systems with significantly better SNR and hence higher margin to FEC thresholds. This would also pave the path toward advanced modulation formats, such as 16-state quadrature amplitude modulation (16QAM), which are frequently used in fiber-optic communication systems. Taken together, these improvements could allow for data rates beyond 100 Gbit/s per channel. Regarding the transmission distance, the demonstrated 58 m is limited only by the available space and could be further increased, e.g., by using higher Tx power levels.

Besides improved performance, a real system implementation would also require a compact integrated Rx assembly. Our experiment already demonstrates compact integration of the photoconductor with the subsequent TIA in a single metal housing, and co-integration with the T-wave amplifiers might be the next step [43]. In the future, the photoconductor might even be combined with advanced photonic circuitry [44,45] into chip-scale optoelectronic T-wave transceiver modules, comprising, e.g., the photonic LO or additional passive optical circuits [9,46].

#### 4. SUMMARY

We showed a first demonstration of a coherent wireless THz communication system using optoelectronic signal processing both at the Tx and at the Rx. Our experiments show that the same Rx concept can be used over a broad frequency range,  $0.03 \text{ THz} \leq f_s \leq 0.340 \text{ THz}$ , spanning more than a decade. We transmit a line rate of 10 Gbit/s using a single T-wave channel at a carrier frequency of 0.31 THz with a BER below the 7% FEC limit. In this experiment, the line rate was limited by the bandwidth of the TIA, but not by the Tx and Rx scheme. We further demonstrate multi-channel transmission using up to 20 carriers with frequencies in the range between 0.287 and 0.325 THz. This leads to an aggregate line rate of 30 Gbit/s with a BER below the threshold for a FEC with 20% overhead. The single- and the multi-channel T-wave link bridges a distance of 58 m, limited by the available space. Our findings demonstrate that coherent T-wave Rx with a widely tunable optoelectronic local oscillator may build the base of a novel class of THz communication systems.

**Funding.** H2020 European Research Council (ERC) (TeraSHAPE, 773248); Deutsche Forschungsgemeinschaft (DFG) (GOSPEL, 403187440); Alfried Krupp von Bohlen und Halbach-Stiftung; Helmholtz International Research School for Teratronics (HIRST); Karlsruhe School of Optics and Photonics (KSOP); Karlsruhe Nano Micro Facility (KNMF).

**Acknowledgment.** The authors thank NTT Electronics (NEL) for providing the UTC-PD for this experiment. Packaging and assembly of the receiver module was supported by Andreas Lipp and Oswald Speck.

See Supplement 1 for supporting content.

#### REFERENCES

1. "Cisco Visual Networking Index: Forecast and Trends, 2017–2022," CISCO White Paper (2017) <https://www.cisco.com/c/en/us/solutions/collateral/service-provider/visual-networking-index-vni/white-paper-c11-741490.pdf>.
2. I. F. Akyildiz, J. M. Jornet, and C. Han, "Terahertz band: next frontier for wireless communications," *Phys. Commun.* **12**, 16–32 (2014).
3. T. S. Rappaport, S. Sun, R. Mayzus, H. Zhao, Y. Azar, K. Wang, G. N. Wong, J. K. Schulz, M. Samimi, and F. Gutierrez, "Millimeter wave mobile communications for 5G cellular: it will work!" *IEEE Access* **1**, 335–349 (2013).
4. A. Kanno, P. T. Dat, N. Yamamoto, and T. Kawanishi, "Millimeter-wave radio-over-fiber network for linear cell systems," *J. Lightwave Technol.* **36**, 533–540 (2018).
5. H.-J. Song and T. Nagatsuma, "Present and future of terahertz communications," *IEEE Trans. Terahertz Sci. Technol.* **1**, 256–263 (2011).
6. T. Nagatsuma, G. Ducourmau, and C. C. Renaud, "Advances in terahertz communications accelerated by photonics," *Nat. Photonics* **10**, 371–379 (2016).
7. G. Ducourmau, P. Szriftgiser, F. Pavanello, E. Peytavit, M. Zakhoune, D. Bacquet, A. Beck, T. Akalin, J.-F. Lampin, and J.-F. Lampin, "THz communications using photonics and electronic devices: the race to data-rate," *J. Infrared Millim. Terahertz Waves* **36**, 198–220 (2015).
8. R. Waterhouse and D. Novak, "Realizing 5G: microwave photonics for 5G mobile wireless systems," *IEEE Microw. Mag.* **16**(8), 84–92 (2015).
9. T. Harter, S. Muehlbrandt, S. Ummethala, A. Schmid, S. Nellen, L. Hahn, W. Freude, and C. Koos, "Silicon-plasmonic integrated circuits for terahertz signal generation and coherent detection," *Nat. Photonics* **12**, 625–633 (2018).
10. D. Pérez, I. Gasulla, and J. Capmany, "Toward programmable microwave photonics processors," *J. Lightwave Technol.* **36**, 519–532 (2018).
11. G. Carpintero, S. Hisatake, D. de Felipe, R. Guzman, T. Nagatsuma, and N. Keil, "Wireless data transmission at terahertz carrier waves generated from a hybrid InP-polymer dual tunable DBR laser photonic integrated circuit," *Sci. Rep.* **8**, 3018 (2018).
12. R. Puerta, J. Yu, X. Li, Y. Xu, J. J. Vegas Olmos, and I. Tafur Monroy, "Single-carrier dual-polarization 328-Gb/s wireless transmission in a D-Band millimeter wave 2×2 MU-MIMO radio-over-fiber system," *J. Lightwave Technol.* **36**, 587–593 (2018).
13. X. Yu, S. Jia, H. Hu, M. Galili, T. Morioka, P. U. Jepsen, and L. K. Oxenlowe, "160 Gbit/s photonics wireless transmission in the 300–500 GHz band," *APL Photon.* **1**, 081301 (2016).
14. S. Koenig, D. Lopez-Diaz, J. Antes, F. Boes, R. Henneberger, A. Leuther, A. Tessmann, R. Schmogrow, D. Hillerkuss, R. Palmer, T. Zwick, C. Koos, W. Freude, O. Ambacher, J. Leuthold, and I. Kallfass, "Wireless sub-THz communication system with high data rate," *Nat. Photonics* **7**, 977–981 (2013).
15. T. Harter, C. Füllner, J. N. Kemal, S. Ummethala, M. Brosi, E. Bründermann, W. Freude, S. Randel, and C. Koos, "110-m THz wireless transmission at 100 Gbit/s using a Kramers-Kronig Schottky barrier diode receiver," in *European Conference on Optical Communication (ECOC)* (2018), paper Th3F.7.
16. S. Jia, X. Pang, O. Ozolins, X. Yu, H. Hu, J. Yu, P. Guan, F. Da Ros, S. Popov, G. Jacobsen, M. Galili, T. Morioka, D. Zibar, and L. K. Oxenlowe, "0.4 THz photonic-wireless link with 106 Gb/s single channel bitrate," *J. Lightwave Technol.* **36**, 610–616 (2018).
17. X. Li, J. Yu, L. Zhao, K. Wang, C. Wang, M. Zhao, W. Zhou, and J. Xiao, "1-Tb/s millimeter-wave signal wireless delivery at D-band," *J. Lightwave Technol.* **37**, 196–204 (2019).
18. H. Shams, T. Shao, M. J. Fice, P. M. Anandarajah, C. C. Renaud, F. Van Dijk, L. P. Barry, and A. J. Seeds, "100 Gb/s multicarrier THz wireless transmission system with high frequency stability based on a gain-switched laser comb source," *IEEE Photon. J.* **7**, 1–11 (2015).
19. T. Harter, M. Weber, S. Muehlbrandt, S. Wolf, J. Kemal, F. Boes, S. Nellen, T. Goebel, J. Giesekeus, T. Zwick, S. Randel, W. Freude, and C. Koos, "Wireless THz communications using optoelectronic techniques for signal generation and coherent reception," in *Conference on Lasers and Electro-Optics (CLEO)* (Optical Society of America, 2017), paper SM3J.2.

20. T. Harter, M. M. H. Adib, S. Wolf, S. Muehlbrandt, M. Weber, M. Blaicher, F. Boes, H. Massler, A. Tessmann, S. Nellen, T. Goebel, J. Giesekus, M. Walther, T. Zwick, W. Freude, S. Randel, and C. Koos, "Wireless multi-subcarrier THz communications using mixing in a photoconductor for coherent reception," in *IEEE Photonics Conference (IPC)* (IEEE, 2017), pp. 147–148.
21. S. Ummethala, T. Harter, K. Koehnle, Z. Li, S. Muehlbrandt, Y. Kutuvantavida, J. N. Kemal, J. Schaefer, H. Massler, A. Tessmann, S. K. Garlapati, A. Bacher, L. Hahn, M. Walther, T. Zwick, S. Randel, W. Freude, and C. Koos, "THz-to-optical conversion in wireless communications using an ultra-broadband plasmonic modulator," *Nat. Photon.* **13**, 519–524 (2019).
22. Y. Salamin, B. Baeuerle, W. Heni, F. C. Abrecht, A. Josten, Y. Fedoryshyn, C. Haffner, R. Bonjour, T. Watanabe, M. Burla, D. L. Elder, L. R. Dalton, and J. Leuthold, "Microwave plasmonic mixer in a transparent fibre-wireless link," *Nat. Photonics* **12**, 749–753 (2018).
23. "Attenuation by atmospheric gases," ITU Recommendation 676-11 (2016).
24. T. Göbel, D. Stanze, B. Globisch, R. J. B. Dietz, H. Roehle, and M. Schell, "Telecom technology based continuous wave terahertz photomixing system with 105 decibel signal-to-noise ratio and 3.5 terahertz bandwidth," *Opt. Lett.* **38**, 4197–4199 (2013).
25. A. Roggenbuck, H. Schmitz, A. Deninger, I. C. Mayorga, J. Hemberger, R. Güsten, and M. Grüniger, "Coherent broadband continuous-wave terahertz spectroscopy on solid-state samples," *New J. Phys.* **12**, 043017 (2010).
26. S. Nellen, B. Globisch, R. B. Kohlhaas, L. Liebermeister, and M. Schell, "Recent progress of continuous-wave terahertz systems for spectroscopy, non-destructive testing, and telecommunication," *Proc. SPIE* **10531**, 105310C (2018).
27. S. Verghese, K. A. McIntosh, S. Calawa, W. F. Dinatale, E. K. Duerr, and K. A. Molvar, "Generation and detection of coherent terahertz waves using two photomixers," *Appl. Phys. Lett.* **73**, 3824 (1998).
28. D. Saeedkia and S. Safavi-Naeini, "Terahertz photonics: optoelectronic techniques for generation and detection of terahertz waves," *J. Lightwave Technol.* **26**, 2409–2423 (2008).
29. Maxim Integrated, "PHY1097," <https://datasheets.maximintegrated.com/en/ds/PHY1097.pdf>.
30. M. R. Billah, M. Blaicher, T. Hoose, P.-I. Dietrich, P. Marin-Palomo, N. Lindenmann, A. Nestic, A. Hofmann, U. Troppenz, M. Moehrle, S. Randel, W. Freude, and C. Koos, "Hybrid integration of silicon photonics circuits and InP lasers by photonic wire bonding," *Optica* **5**, 876–883 (2018).
31. H. Ito, T. Furuta, Y. Muramoto, T. Ito, and T. Ishibashi, "Photonic millimetre- and sub-millimetre-wave generation using J-band rectangular-waveguide-output uni-travelling-carrier photodiode module," *Electron. Lett.* **42**, 1424–1425 (2006).
32. A. Tessmann, A. Leuther, V. Hurm, H. Massler, S. Wagner, M. Kuri, M. Zink, M. Riessle, H.-P. Stulz, M. Schlechtweg, and O. Ambacher, "A broadband 220–320 GHz medium power amplifier module," in *IEEE Compound Semiconductor Integrated Circuit Symposium (CSICS)* (IEEE, 2014).
33. A. W. Mohammad, H. Shams, K. Balakier, C. Graham, M. Natrella, A. J. Seeds, and C. C. Renaud, "5 Gbps wireless transmission link with an optically pumped uni-traveling carrier photodiode mixer at the receiver," *Opt. Express* **26**, 2884–2890 (2018).
34. A. W. Mohammad, H. Shams, C. P. Liu, C. Graham, M. Natrella, A. J. Seeds, and C. C. Renaud, "60-GHz transmission link using uni-traveling carrier photodiodes at the transmitter and the receiver," *J. Lightwave Technol.* **36**, 4507–4513 (2018).
35. J. Ma, N. J. Karl, S. Bretin, G. Ducournau, and D. M. Mittleman, "Frequency-division multiplexer and demultiplexer for terahertz wireless links," *Nat. Commun.* **8**, 729 (2017).
36. M. Yata, M. Fujita, and T. Nagatsuma, "Photonic-crystal diplexers for terahertz-wave applications," *Opt. Express* **24**, 7835–7849 (2016).
37. M. Giovanni and L. Frecassetti, "E-band and V-band - survey on status of worldwide regulation," in *ETSI White Paper* (2015).
38. F. Boes, J. Antes, T. Messinger, D. Meier, R. Henneberger, A. Tessmann, and I. Kalfass, "Multi-gigabit E-band wireless data transmission," in *IEEE MTT-S International Microwave Symposium (IMS)* (2015).
39. A. de J. Fernandez Olvera, A. Roggenbuck, K. Dutzi, N. Vieweg, H. Lu, A. C. Gossard, and S. Preu, "International system of units (SI) traceable noise-equivalent power and responsivity characterization of continuous wave ErAs:InGaAs photoconductive terahertz detectors," *Photonics* **6**, 15 (2019).
40. S. Muehlbrandt, A. Melikyan, T. Harter, K. Köhnle, A. Muslija, P. Vincze, S. Wolf, P. Jakobs, Y. Fedoryshyn, W. Freude, J. Leuthold, C. Koos, and M. Kohl, "Silicon-plasmonic internal-photoemission detector for 40 Gbit/s data reception," *Optica* **3**, 741–747 (2016).
41. H.-J. Song, "Packages for terahertz electronics," *Proc. IEEE* **105**, 1121–1138 (2017).
42. Semtech, "Transimpedance amplifier GN1081," <https://www.semtech.com/products/signal-integrity/transimpedance-amplifiers/gn1081>.
43. K. Sengupta, T. Nagatsuma, and D. M. Mittleman, "Terahertz integrated electronic and hybrid electronic-photonic systems," *Nat. Electron.* **1**, 622–635 (2018).
44. A. H. Atabaki, S. Moazeni, F. Pavanella, H. Gevorgyan, J. Notaros, L. Alloatti, M. T. Wade, C. Sun, S. A. Kruger, H. Meng, K. Al Qubaisi, I. Wang, B. Zhang, A. Khilo, C. V. Baiocco, M. A. Popović, V. M. Stojanović, and R. J. Ram, "Integrating photonics with silicon nanoelectronics for the next generation of systems on a chip," *Nature* **556**, 349–354 (2018).
45. L. M. Augustin, R. Santos, E. den Haan, S. Kleijn, P. J. A. Thijs, S. Latkowski, D. Zhao, W. Yao, J. Bolk, H. Ambrosius, S. Mingaleev, A. Richter, A. Bakker, and T. Korthorst, "InP-based generic foundry platform for photonic integrated circuits," *IEEE J. Sel. Top. Quantum Electron.* **24**, 6100210 (2018).
46. G. Carpintero, K. Balakier, Z. Yang, R. C. Guzman, A. Corradi, A. Jimenez, G. Kervella, M. J. Fice, M. Lamponi, M. Chitoui, F. van Dijk, C. C. Renaud, A. Wonfor, E. A. J. M. Bente, R. V. Penty, I. H. White, and A. J. Seeds, "Microwave photonic integrated circuits for millimeter-wave wireless communications," *J. Lightwave Technol.* **32**, 3495–3501 (2014).